

GUIDEFILL: GPU ACCELERATED, ARTIST GUIDED GEOMETRIC INPAINTING FOR 3D CONVERSION*

L. ROBERT HOCKING[†], RUSSELL MACKENZIE[‡], AND CAROLA-BIBIANE SCHÖNLIEB[§]

Abstract. The conversion of traditional film into stereo 3D has become an important problem in the past decade. One of the main bottlenecks is a disocclusion step, which in commercial 3D conversion is usually done by teams of artists armed with a toolbox of inpainting algorithms. A current difficulty in this is that most available algorithms are either too slow for interactive use, or provide no intuitive means for users to tweak the output.

In this paper we present a new fast inpainting algorithm based on transporting along automatically detected splines, which the user may edit. Our algorithm is implemented on the GPU and fills the inpainting domain in successive shells that adapt their shape on the fly. In order to allocate GPU resources as efficiently as possible, we propose a parallel algorithm to track the inpainting interface as it evolves, ensuring that no resources are wasted on pixels that are not currently being worked on. Theoretical analysis of the time and processor complexity of our algorithm without and with tracking (as well as numerous numerical experiments) demonstrate the merits of the latter.

Our transport mechanism is similar to the one used in coherence transport [7, 22], but improves upon it by corrected a “kinking” phenomena whereby extrapolated isophotes may bend at the boundary of the inpainting domain. Theoretical results explaining this phenomena and its resolution are presented.

Although our method ignores texture, in many cases this is not a problem due to the thin inpainting domains in 3D conversion. Experimental results show that our method can achieve a visual quality that is competitive with the state-of-the-art while maintaining interactive speeds and providing the user with an intuitive interface to tweak the results.

Key words. image processing, image inpainting, 3D conversion, PDEs, parallel algorithms, GPU

AMS subject classifications. 68U10, 68W10, 65M15

1. Introduction. Overview and Motivation. The increase in demand over the past decade for 3D content has resulted in the emergence of a multi-million dollar industry devoted to the conversion of 2D films into stereo 3D. This is partly driven by the demand for 3D versions of old films, but additionally many current filmmakers are choosing to shoot in mono and convert in post production [32]. Examples of recent films converted in whole or in part include Maleficent, Thor, and Guardians of the Galaxy [1].

Mathematically, 3D conversion amounts to constructing the image or video shot by a camera at the perturbed position $p + \delta p$ and orientation $O + \delta O$, given the footage at (p, O) . Broadly speaking this is accomplished via a process for “warping” the original image based known or estimated camera parameters, combined with a known or estimated depth map [39]. While multiple pipelines are possible, one thing they all have in common is a hole-filling or disocclusion step whereby missing information in the form of geometry visible from $(p + \delta p, O + \delta O)$ but not from (p, O) is “inpainted”.

*Submitted to the editors May 18, 2022.

Funding: LRH acknowledges support from the Cambridge Commonwealth Trust and the Cambridge Center for Analysis. CBS acknowledges support from Leverhulme Trust project on Breaking the non-convexity barrier, EPSRC grant Nr. EP/M00483X/1, the EPSRC Centre Nr. EP/N014588/1 and the Cantab Capital Institute for the Mathematics of Information.

[†]Department of Applied Mathematics and Theoretical Physics, University of Cambridge (lrh30@cam.ac.uk).

[‡]Gener8 Media corp, (russell@gener8.com).

[§]Department of Applied Mathematics and Theoretical Physics, University of Cambridge, (cbs31@cam.ac.uk).

This step is considered one of the most technical and time consuming pieces of the pipeline [32].

In theory inpainting may be done automatically by any of a multitude of image/video inpainting algorithms that exist (we will review the state of the art in a moment). In practice, however, no one method is adequate for every situation, and inpainting is done by teams of artists armed a “toolbox” of inpainting algorithms. These algorithms provide a starting point which artists may then touch up by hand.

Image and Video Inpainting. Image inpainting refers to the filling in of a region in an image called the inpainting domain in such a way that the result looks plausible to the human eye.

Image inpainting methods can loosely be categorized as *exemplar-based* and *geometric*. The former generally operate based on some procedure for copying patches of the undamaged portion of the image into the inpainting domain, either in a single pass from the boundary inwards as in Criminisi et al. [14], or iteratively as in Wexler et al. [37] and Arias et al. [3]. The choice of which patch or patches to copy into a given area of the inpainting domain is decided using a nearest neighbor search based on a patch similarity metric. Originally prohibitively expensive, a breakthrough was made in the PatchMatch algorithm [4], which provides a fast *approximate* nearest neighbor search. PatchMatch is used behind the scenes in the Photoshop’s famous *Content-Aware Fill* tool. On the other hand, geometric inpainting methods aim to smoothly extend image structure into the inpainting domain, typically using partial differential equations or variational principals. Continuation may be achieved by either *interpolation* or *extrapolation*. Examples of methods based on interpolation include the seminal work of Bertalmio et al. [5], TV, TV- H^{-1} , Mumford-Shah, Cahn-Hilliard inpainting [12, 8] and Euler’s Elastica [23, 11]. These approaches are typically iterative and convergence is often slow, implying that such methods are usually not suitable for real-time applications. Telea’s algorithm [34] and coherence transport [7, 22] (which can be thought of as an improvement of the former) are based on *extrapolation* and visit each pixel only once, filling them in order according to their distance from the boundary of the inpainting domain. Unlike their iterative counterparts, these two methods are both very fast, while possibly creating an unfeasible “seam” in the center of the inpainting domain where the separate extrapolations from different sides meet. See also [31] for a comprehensive survey of geometric inpainting methods.

Geometric methods are designed to propagate structure, but fail to reproduce texture. Similarly, exemplar-based approaches excel at reproducing texture, but are limited in terms of their ability to propagate structure. A few attempts have been made at combining geometric and exemplar-based methods, such as Cao et. al [10], which gives impressive results but is relatively expensive.

Video inpainting adds an additional layer of complexity, because now temporal information is available, which is exploited by different algorithms in different ways. For example, when inpainting a moving object in the foreground, one can expect to find the missing information in nearby frames - this type of strategy is utilized in for example [19]. Another, more general strategy is to generalize exemplar-based image inpainting methods to video by replacing 2D image patches with 3D spacetime cubes. This approach is taken in [24, 25], which also present a generalized patch-match algorithm for video. While producing impressive results, this method is also very expensive, both in terms of time and space complexity (see Section 5). Finally, the authors of [17] present a strategy for video inpainting of planar or almost-planar surfaces, based on inpainting a single frame and then propagating the result to neigh-

boring frames using an estimated homography.

Related Work. Over the past decade there has been a considerable amount of work devoted to designing algorithms for automatic or semi-automatic 3D conversion. In regards to the hole filling step, there is great variability in how it is handled. At one extreme are cheap methods that inpaint each frame independently using very basic rules such as clamping to the color of the nearest useable pixel [20], or taking a weighted average of closest useable pixels along a small number (8 – 12) of fixed directions [40, 16]. Slightly more sophisticated is the approach in [27] which applies a depth-adapted variant of Telea’s algorithm [34]. At the other extreme are expensive methods taking temporal information explicitly into account, such as [13] which copies spacetime patches into the inpainting domain via a process similar to Criminisi et al. Also towards the expensive end of the spectrum are exemplar-based approaches which inpaint each frame independently using depth-adapted variants of Criminisi et al, such as [38].

Our Contribution. What appears to be missing is an algorithm suitable for the “middle ground” of cases where Telea’s algorithm and coherence transport are inadequate, but exemplar-based approaches are needlessly expensive. In particular, because the inpainting domains in 3D conversion tend to be thin “cracks” (see Figure 1), there are many situations in which one can safely ignore texture.

In this paper we present a fast, non-texture based, user guided inpainting algorithm intended for use by artists for the hole-filling step of 3D conversion. We have designed our algorithm with two goals in mind:

- The method retains interactive speeds even when applied to the HD footage used in film.
- Although the method is automatic, the artist is kept “in the loop” with a means of possibly adjusting the result of inpainting that is *intuitive* (that is, they are not simply adjusting parameters)¹.

The first of these goals is accomplished via an efficient GPU implementation based on a novel algorithm for tracking the boundary of the inpainting domain as it evolves. Since our method only operates on the boundary of the inpainting domain on any given step, knowing where the boundary is means that we can assign GPU processors only to boundary pixels, rather than all pixels in the image. For very large images ($\sqrt{N} \gg p$, where N denotes the number of pixels in the inpainting domain, and p denotes the number of available processors), our tracking algorithm leads to a time and processor complexity of $T(N, M) = O(N \log N)$, $P(N, M) = O(\sqrt{N} + M)$ respectively (where $N + M$ is the total number of pixels in the image), versus $T(N, M) = O((N + M)\sqrt{N})$, $P(N, M) = O(N + M)$ without tracking - see Theorem 3 and Theorem 4. Moreover, for moderately large problems ($\sqrt{N} \lesssim p$ and $N + M \gg p$) the gains are larger - $T(N, M) = O(\sqrt{N} \log N)$ with tracking in this case.

The second goal is accomplished by providing the user with automatically computed splines showing how key image isophotes are to be extended. These splines may be edited if necessary.

Our method - which we call Guidefill - is intended as a practical tool that is fast and flexible, and applicable to many, but not all, situations. It is not intended as a

¹It is worth mentioning that there are at least two inpainting algorithms in the literature aimed at giving the user intuitive control, namely Sun et al [33] and Barns et al. [4] (both are exemplar-based). But the former of these is relatively expensive and the latter, while less expensive, is limited to linear edges. As far as we know our method is the first *geometric* method to give the user the ability to influence the result of inpainting.

black box capable of providing the correct result in any situation given enough time. Our method was originally designed for the 3D conversion company Gener8 and a version of it is in use by their stereo artists.

Guidefill is inspired by coherence transport [7, 22], and is similar to it in that both methods operate by measuring the orientation of image isophotes in the undamaged region and then extrapolating based on a transport mechanism. However, the method by which we solve these separate subproblems is very different from [7, 22]. In particular, we will show that the transport mechanism in coherence transport, when fed a desired transport direction \mathbf{g} , instead transports along a direction \mathbf{g}^* such that $\mathbf{g}^* \neq \mathbf{g}$ unless \mathbf{g} points in one of a small number of special directions. The result is “kinking” of extrapolated isophotes (see Figures 5, 7). This behaviour, which the authors of [7, 22] appear unaware of (the theory in [7] does not account for it), is explored in Section 3.2. We present an improved transport mechanism overcoming this problem, as well as a theoretical explanation of its origin and resolution - see Theorem 1. Additional details on the similarities and differences between our method and coherence transport [7, 22] are presented in Section 3.

Similarly to many state of the art 3D conversion approaches we treat the problem frame by frame. While an extension that uses temporal information would be interesting (and is a direction we would like to explore in the future), it is outside of the scope of this paper.

Organization. In Section 2 we go over a 3D conversion pipeline commonly used in film. Alternatives not used in film are also touched on. Next, in Section 3 we present our proposed method, including details of two possible GPU implementations. A theoretical explanation of the kinking phenomena exhibited by coherence transport is also provided in Section 3.2. In Section 4 we analyze the time complexity and processor complexity of our method as a parallel algorithm. In Section 5 we show the results of our method applied to a series of 3D conversion examples. Results are compared with competing methods both in terms of runtime and visual quality. At the same time, we also validate the complexity analysis of Section 4. Finally, in Section 6 we draw some conclusions.

Notation.

- $h =$ the width of one pixel.
- $\mathbb{Z}_h^2 := \{(nh, mh) : (n, m) \in \mathbb{Z}^2\}$.
- Given $\mathbf{x} \in \mathbb{R}^2$, we denote by $\theta(\mathbf{x}) \in [0, 2\pi)$ the counter-clockwise angle \mathbf{x} makes with the x-axis.
- $\Omega = [a, b] \times [c, d]$ and $\Omega_h = \Omega \cap \mathbb{Z}_h^2$ are the continuous and discrete image domains.
- $D_h \subset \Omega_h$ is the discrete inpainting domain.
- $B_h \subset \Omega_h \setminus D_h$ is the set of “bystander pixels” (defined in Section 2.1) that are neither inpainted nor used for inpainting.
- $u_h : \Omega_h \setminus (D_h \cup B_h) \rightarrow \mathbb{R}^d$ is the given image (video frame).
- $D \subset \Omega := \{\mathbf{x} \in \Omega : \exists \mathbf{y} \in D_h \text{ s.t. } \|\mathbf{y} - \mathbf{x}\|_\infty < h\}$ is the continuous inpainting domain.
- $B \subset \Omega$ is the continuous bystander set, defined in terms of B_h in the same way as D .
- $\mathbf{g} : D_h \rightarrow \mathbb{R}^2$ is the guidefield used to guide the inpainting.
- $B_{\epsilon, h}(\mathbf{x}) = \{\mathbf{y} \in \Omega_h : \|\mathbf{x} - \mathbf{y}\| \leq \epsilon\}$.
- $\hat{B}_{\epsilon, h}(\mathbf{x}) = R(B_{\epsilon, h}(\mathbf{x}))$, where R is the rotation matrix taking $(0, 1)$ to $\mathbf{g}(\mathbf{x})$.

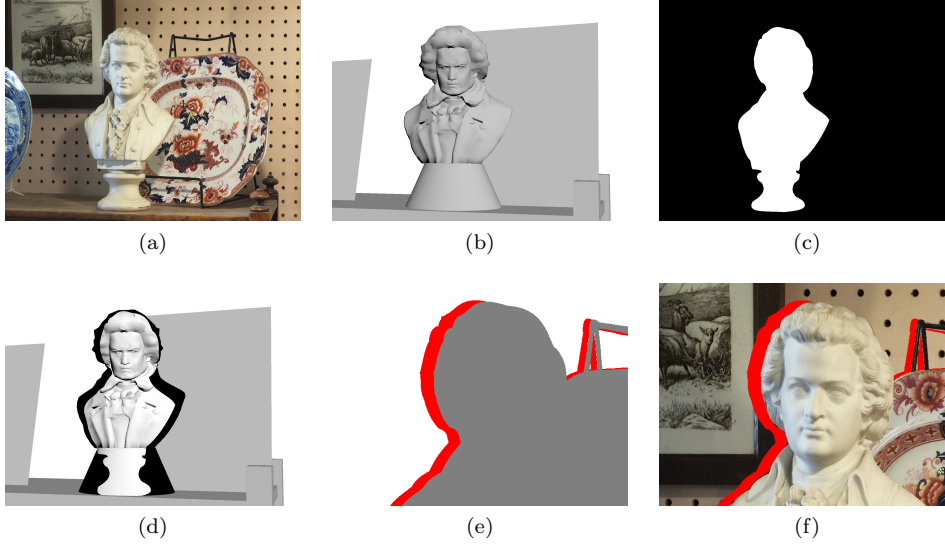


Fig. 1: Intermediate data generated in a 3D conversion pipeline prior to inpainting: (a) original image, (b) rough 3D geometry, (c) object mask, (d) projection of a object mask onto the corresponding object geometry, (e) example labeling of pixels in the image according to object and visibility (in this case the object in question is the wall, white pixels are visible from both viewpoints, red are visible from the new viewpoint but occluded in the original view, grey are occluded in both views), (f) the generated new view with red “cracks” requiring inpainting.

- $\mathcal{N}(\mathbf{x}) = \{\mathbf{x} + \mathbf{y} : \mathbf{y} \in \{-h, 0, h\} \times \{-h, 0, h\}, \mathbf{y} \neq \mathbf{0}\}$ is the eight-point neighborhood of \mathbf{x} .
- Given $A_h \subset \mathbb{Z}_h^2$, we define the discrete (inner) boundary of A_h by

$$\partial A_h := \{\mathbf{x} \in A_h : \mathcal{N}(\mathbf{x}) \cap \mathbb{Z}_h^2 \setminus A_h \neq \emptyset\}.$$

For convenience we typically drop the word “inner” and refer to ∂A_h as just the boundary of A_h .

- Given $A_h \subset \mathbb{Z}_h^2$, we define the discrete *outer* boundary of A_h by

$$\partial_{\text{outer}} A_h := \{\mathbf{x} \in \mathbb{Z}_h^2 \setminus A_h : \mathcal{N}(\mathbf{x}) \cap A_h \neq \emptyset\}.$$

2. A 3D Conversion Pipeline. 3D conversion amounts to constructing, for each frame in a video, a stereo pair of left and right eye images. Here we briefly review a 3D conversion pipeline commonly used in film - see for example [39] for a more detailed description. Note also that other pipelines are possible, as for example the pipelines proposed for 3D TV in [27, 16].

The pipeline relevant to us involves three main steps (typically done by separate teams of specialized artists) which must be completed before inpainting can proceed:

1. If camera data (including position, orientation and field of view) is not known, it must be estimated. This process is often called “match-move” and is typically done with the aid of semi-automatic algorithms based on point tracking [30, 15].

2. Accurate masks must be generated for all objects and for every frame (See Figure 1(c)). This is typically done to a subpixel accuracy using editable Bézier splines called “roto”. These are effectively used to generate the depth discontinuities visible from the new viewpoint(s) and need to be as accurate as possible [32].
3. A plausible 3D model of the scene must be generated (see Figure 1(b) for an example). This will effectively be used to generate the “smooth” component of the depth map as viewed from the new viewpoint(s) and does not have to be perfect. It is however very important that each object’s mask generated in the previous step fit entirely onto its geometry when projected from the assumed camera position, as in Figure 1(d). For this reason 3D geometry is typically designed to be slightly larger than it would be in real life [39].
4. For each object, a multi-label mask must be generated assigning a label to each pixel in the image as either
 - belonging to the object and visible from the original viewpoint, or
 - belonging to the object and occluded in the original viewpoint, but visible in the new viewpoint, or
 - belonging to the object and occluded in both the original and new viewpoints, or
 - belonging to another object.

See Figure 1(e) for an example where the four labels are colored white, red, grey, and black respectively, and the object in question is the background wall.

Once these components are in place, the original footage, clipped using the provided masks, is projected onto the geometry from the assumed camera position and orientation. The new view is then generated by rendering the 3D scene from the perspective of a new virtual camera. This new view, however, contains disoccluded regions - formerly hidden by geometry in the old view - which must be inpainted (see Figure 1(f)). Inpainting then proceeds on an object by object basis, with each object inpainted separately.

2.1. Bystander Pixels. In most image inpainting algorithms it is assumed that all pixels in $\Omega_h \setminus D_h$ may be used for inpainting. However, for this application each object is inpainted separately, so some of the pixels in $\Omega_h \setminus D_h$ belong to other objects (according to the labelling in step 4) and should be excluded. Failure to do so will result in “bleeding” artifacts, where, for example, a part of a foreground object is extended into what is supposed to be a revealed area of background - see Figure 2.

Pixels which are neither inpainted nor used as inpainting data are called “bystander pixels”, and the set of all such pixels is denoted by B_h . Pixels in $\Omega_h \setminus (D_h \cup B_h)$ are called “readable”.

2.2. Alternative Pipelines. It is worth mentioning that many conversion pipelines do not have a labelling step such as step 4 above, and instead rely on imperfect heuristics to decide which pixels should be used for inpainting. For example, one common heuristic which is used in [27, 38] first divides the inpainting domain into a series of horizontal line segments. For each line segment, the depth of the pixels at the left and right endpoints are compared, the pixel with the greater depth is declared part of the “background” and used for inpainting, while the other pixel is declared “foreground” and discarded. A similar approach, used in [40, 16], is to pass a number of lines through each pixel in the inpainting domain. Each line will intersect the boundary in two places, as they are terminated once they reach the boundary.

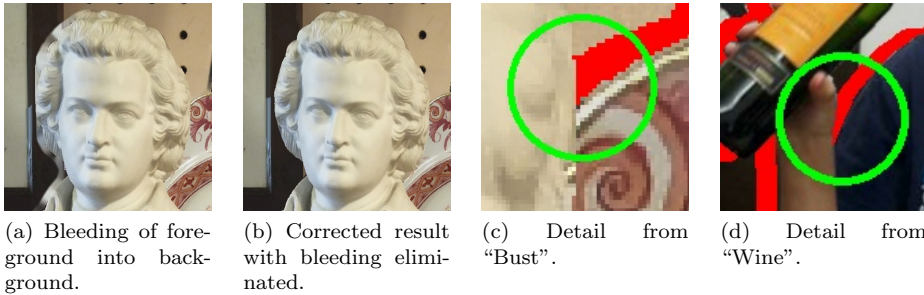


Fig. 2: Importance of the pixel labeling step in the 3D conversion pipeline and failure cases for alternative 3D conversion pipelines: When the new view from Figure 1(f) is inpainted using *all* pixels not in the inpainting domain (that is, both the pixels colored white and the pixels colored grey in Figure 1(e)), we get bleeding of the foreground into the background as in (a). When we inpaint using only pixels labelled as belonging to the current object (the white pixels in Figure 1(e)), we get the improved result in (b). Some 3D conversion pipelines assume that the inpainting domain consists of horizontal line segments with foreground on one side and background on the other. However, the circled areas in (c)-(d) have foreground pixels on both sides. Algorithms based on this assumption (e.g. [27, 38, 40, 16] will result in bleeding of the foreground into the background in these areas, similar to (a).

As before, the point of intersection with the larger depth value is declared to be “background” and used for inpainting while the closer pixel is labelled foreground and discarded.

These approaches have an advantage in that they avoid the need to carry out a costly labelling step, making them useful for applications where realtime performance is a must. However, it is not difficult to find examples of failure cases for these heuristics - two such examples are shown in Figure 2(c)-(d), where we have circled areas where the use of these heuristics will result in foreground being mislabelled as background, leading to bleeding artifacts similar to Figure 2(a). Due to these issues we believe that these alternative pipelines are not suitable for film, and indeed case studies such as [39] indicate that they are not typically used in the effects industry.

3. Proposed Approach. Guidefill is a member of an extremely simple class of inpainting algorithms which also contains coherence transport [7, 22] and Telea’s algorithm [34]. These methods fill the inpainting domain in successive shells from the boundary inwards, with the color of a given pixel due to be filled computed as a weighted average of its already filled neighbors. As the algorithm proceeds, the inpainting domain shrinks, generating a sequence of inpainting domains $D_h = D_h^{(1)} \supset D_h^{(2)} \supset \dots \supset D_h^{(K)} = \emptyset$. At iteration k , only pixels belonging to $\partial D_h^{(k)}$ are filled, however, $\partial D_h^{(k)}$ is not typically filled in its entirety. In particular, boundary pixels are required to have at least one neighbor in $\Omega_h \setminus (D_h \cup B_h)$ (in other words, at least one “readable” neighbor) before they are eligible to be filled. This is a minimum requirement and they may be made to wait until additional conditions are satisfied before they are “ready” to be filled (see Section 3.4). Algorithm 1 illustrates this with pseudo code. While very basic, these methods have the advantage of being cheap

Algorithm 1 Shell Based Geometric Inpainting

```

 $u_h$  = image
 $D_h$  = inpainting domain
 $\partial D_h$  = inpainting domain boundary
 $B_h$  = bystander pixels
while  $D_h \neq \emptyset$  do
  for  $\mathbf{x} \in \partial D_h$  do
    if ready( $\mathbf{x}$ ) then
       $u_h(\mathbf{x}) = (\text{Weighted})$  average of neighbors in  $\Omega_h \setminus (D_h \cup B_h)$ 
    end if
  end for
   $A = \{\mathbf{x} \in \partial D_h : \text{ready}(\mathbf{x})\}$ 
   $D_h = D_h \setminus A$ 
end while

```

and highly parallelizable. In particular, when implemented on the GPU the entire boundary of the inpainting domain can be filled in parallel. If done carefully, this yields a very fast algorithm suitable for very large images - see Section 3.5.

Guidefill is inspired in part by coherence transport [7, 22]. Coherence transport operates by adapting its weights in order to extrapolate along isophotes in the undamaged portion of the image when they are detected, and applying a smooth blur when they are not. While relatively fast and achieving good results in many cases, it has a number of drawbacks:

1. Users may need to tune parameters in order to obtain a good result.
2. Extrapolated isophotes may “kink” (see Figure 5 and Section 3.2).
3. The method is a black box with no artist control.
4. The implementation in [7, 22] is sequential, failing to exploit the inherent parallelizability of the approach.
5. The quality of the result can be strongly influenced by the order in which pixels are filled - see Figure 8. This is partially addressed in [22], where several methods are proposed for precomputing improved pixel orderings based on non-euclidean distance functions. However, these methods all either require manual intervention or else have other disadvantages - see Section 3.4.

Guidefill is aimed at overcoming these difficulties while providing an efficient GPU implementation, in order to create a tool for 3D conversion providing intuitive artist control and improved results.

3.1. Overview. The main idea behind Guidefill is to generate, possibly based on user input, a suitable vector field $\mathbf{g} : D_h \rightarrow \mathbb{R}^2$ to guide the inpainting process, prior to inpainting. The vector field \mathbf{g} , which we call the “guide field”, is generated based on a small set of curves carrying information about how key image edges in $\Omega_h \setminus (D_h \cup B_h)$ should be continued into D_h . These curves provide an intuitive mechanism by which the user can influence the results of inpainting (see Figure 3).

Coherence transport also utilizes a vector field $\mathbf{g}(\mathbf{x})$, but it is calculated concurrently with inpainting. Precomputing the guide field ahead of time is an advantage because the guide field contains information that can be used to automatically compute a good pixel ordering, avoiding artifacts such as Figure 8. Given any pixel $\mathbf{x} \in \partial D_h$ due to be filled, our algorithm decides based on $\mathbf{g}(\mathbf{x})$ whether to allow \mathbf{x} to be filled, or to wait for a better time. Our test amounts to checking whether or

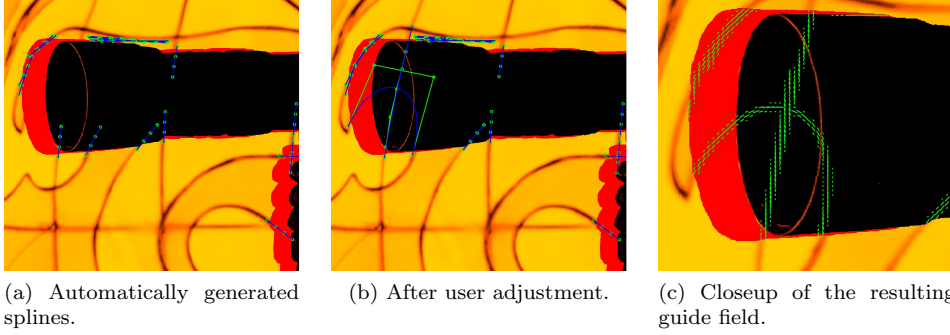


Fig. 3: Generating the guide field \mathbf{g} (c) based on splines automatically generated by Guidefill (a) and edited by the user (b).

not enough pixels have already been inpainted in the area pointed to by $\mathbf{g}(\mathbf{x})$, and is discussed in greater detail in Section 3.4.

The method begins with the user either drawing the desired edges directly onto the image as Bézier splines using a GUI, or else by having a set of splines automatically generated for them based on the output of a suitable edge detection algorithm run on $\Omega_h \setminus (D_h \cup B_h)$. In the latter case the user may either accept the result or else use it as a starting point which they may improve upon by editing and/or removing existing splines as well as drawing new ones. This is illustrated in Figure 3.

Next, the idea is to choose $\mathbf{g}(\mathbf{x})$ to be $\mathbf{0}$ when \mathbf{x} is far away from any splines (e.g. more than a small number of pixels, around ten by default), and “parallel” to the splines when \mathbf{x} is close. More precisely, we define a “spline distance map” $T_h^B(\mathbf{x})$ which gives the orthogonal distance from \mathbf{x} to the closest spline to \mathbf{x} . Then the direction of $\mathbf{g}(\mathbf{x})$ is given by $\nabla^\perp T_h^B(\mathbf{x})$ while the magnitude is an exponentially decreasing function of $T_h^B(\mathbf{x})$.

The purpose of the guidefield is to ensure that the inpainting will tend to follow the splines wherever they are present. To accomplish this, a given pixel $\mathbf{x} \in \partial D_h$ due to be inpainted is “filled” by assigning it a color equal to a weighted average of its already filled neighbors, with weights biased in favor of neighboring pixels \mathbf{y} such that $\mathbf{y} - \mathbf{x}$ is parallel to $\mathbf{g}(\mathbf{x})$. This is accomplished using the weight function

$$(3.1) \quad w(\mathbf{x}, \mathbf{y}) = \frac{1}{\|\mathbf{y} - \mathbf{x}\|} \exp\left(-\frac{\mu^2}{2\epsilon^2} (\mathbf{g}^\perp(\mathbf{x}) \cdot (\mathbf{y} - \mathbf{x}))^2\right),$$

(introduced in [7]) where μ and ϵ are positive parameters. The color $u_h(\mathbf{x})$ is then computed as

$$(3.2) \quad u_h(\mathbf{x}) = \frac{\sum_{\mathbf{y} \in \tilde{B}_{\epsilon,h}(\mathbf{x}) \cap \Omega \setminus D} w(\mathbf{x}, \mathbf{y}) u_h(\mathbf{y})}{\sum_{\mathbf{y} \in \tilde{B}_{\epsilon,h}(\mathbf{x}) \cap \Omega \setminus D} w(\mathbf{x}, \mathbf{y})}.$$

This formula is similar to the one used by coherence transport [7], where the same weights are used but the guidefield is computed differently. However, whereas the sum in coherence transport is taken over the filled portion of the discrete ball $B_{\epsilon,h}(\mathbf{x})$ aligned with the image lattice, we sum over the available “pixels” within a *rotated* ball $\tilde{B}_{\epsilon,h}(\mathbf{x})$ aligned with the local guide direction $\mathbf{g}(\mathbf{x})$ - see Figure 4 for an illustration.

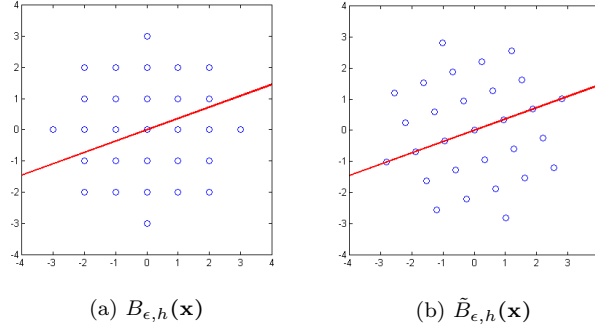


Fig. 4: Illustration of the discrete ball $B_{\epsilon,h}(\mathbf{x})$ used by coherence transport and the rotated ball $\tilde{B}_{\epsilon,h}(\mathbf{x})$ used by Guidefill. The ball $\tilde{B}_{\epsilon,h}(\mathbf{x})$ is rotated so that it is aligned with the line L passing through \mathbf{x} parallel to $\mathbf{g}(\mathbf{x})$ (L is shown in red). In general $\tilde{B}_{\epsilon,h}(\mathbf{x})$ contains “ghost pixels” lying between pixel centers, which are defined using bilinear interpolation of their “real” pixel neighbors.

This means that we will in general be evaluating u_h *between* pixel centers, which we accomplish by extending the domain of u_h from $\Omega_h \setminus (D_h \cup B_h)$ to $\Omega \setminus (D \cup B)$ using bilinear interpolation. That is, we define

$$(3.3) \quad u_h(\mathbf{x}) = \sum_{\mathbf{y} \in \Omega_h} \Lambda_{\mathbf{y},h}(\mathbf{x}) u_h(\mathbf{y}) \quad \text{for all } \mathbf{x} \in \Omega \setminus (D \cup B),$$

where $\{\Lambda_{\mathbf{y},h}\}_{\mathbf{y} \in \Omega_h}$ denotes the basis functions of bilinear interpolation. Note that the continuous sets B and D have been defined so that they include a one pixel wide buffer zone around their discrete counterparts, ensuring that bilinear interpolation is well defined outside $D \cup B$. The reason for the introduction of $\tilde{B}_{\epsilon,h}(\mathbf{x})$ is discussed in the next Section.

3.2. Resolving Kinking Artifacts using Ghost Pixels. Figure 5 illustrates the use of coherence transport and Guidefill - each with $\epsilon = 3\text{px}$ and $\mu = 50$ - for connecting a pair of broken lines. When the line to be extrapolated is vertical ($\theta = 90^\circ$), both methods are successful. However, when the line is rotated slightly ($\theta = 73^\circ$) coherence transport causes the extrapolated line to “kink”, whereas Guidefill makes a successful connection. This happens because coherence transport is trying to bias inpainting in favor of those pixels $\mathbf{y} \in B_{\epsilon,h}(\mathbf{x})$ sitting on the line L passing through \mathbf{x} in the direction $\mathbf{g}(\mathbf{x})$, but in this case $B_{\epsilon,h}(\mathbf{x})$ contains no such pixels - see Figure 4(a). Instead coherence transport favors the pixel(s) *closest* to L , which in this case happens to be $\mathbf{y} = \mathbf{x} + (0, h)$. Since $\mathbf{y} - \mathbf{x}$ is in this case parallel to $(0, 1)$, isophotes are extrapolated along this direction instead of along $\mathbf{g}(\mathbf{x})$ as desired. This implies that inpainting can only be expected to succeed when $\mathbf{g}(\mathbf{x})$ is of the form $\mathbf{g}(\mathbf{x}) = (\lambda n, \lambda m)$ for $\lambda \in \mathbb{R}$, $n, m \in \mathbb{Z}$ and $n^2 + m^2 \leq 9$ (only a finite number of directions).

We resolve this problem by replacing $B_{\epsilon,h}(\mathbf{x})$ with the rotated ball of ghost pixels $\tilde{B}_{\epsilon,h}(\mathbf{x})$, which is constructed in order to contain at least one “pixel” on L besides \mathbf{x} , as illustrated in Figure 4(b).

In Figure 6 we also illustrate the importance of ghost pixels on a non-synthetic example with a smoothly varying guide field (Figure 3). When ghost pixels are not

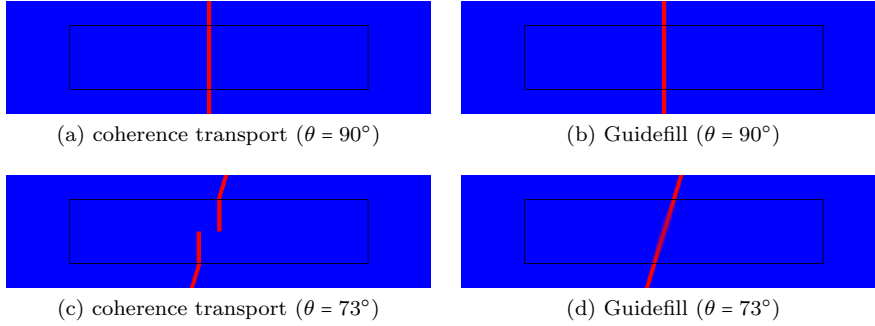


Fig. 5: Connecting a broken lines using coherence transport (left column) and Guidefill (right column). When the line to be extrapolated is vertical ($\theta = 90^\circ$), both methods are successful. However, when the line is rotated slightly ($\theta = 73^\circ$) coherence transport causes the extrapolated line to “kink”, whereas Guidefill continues to produce a satisfactory result. A theoretical explanation for this phenomena is provided in Theorem 1 and illustrated in Figure 7. In this case ($\epsilon = 3\text{px}$), Theorem 1 predicts that for $0 \leq \theta(\mathbf{g}) \leq \pi/2$, coherence transport exhibits kinking unless $\theta \in \{\arctan(0.5), \pi/4, \arctan(2), \pi/2\}$. On the other hand, Guidefill exhibits no kinking provided $\theta > \arcsin(1/3)$.

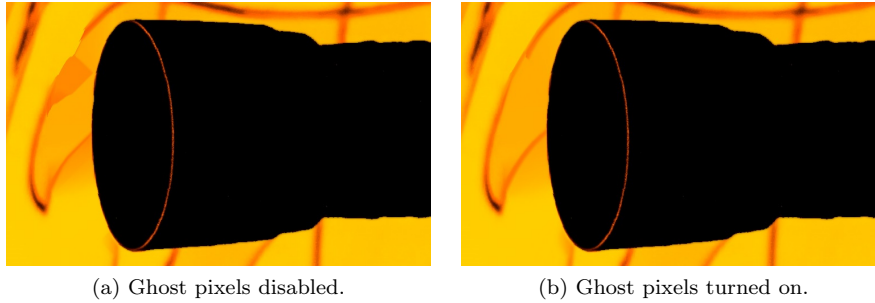


Fig. 6: The effect of ghost pixels on a non-synthetic example ($\epsilon = 3\text{px}$, $\mu = 50$). When ghost pixels are disabled, the extrapolated isophotes are unable to smoothly curve as only finitely many transport directions are possible.

used, the extrapolated isophotes are unable to smoothly curve as only finitely many transport directions are possible. The result is a break in the extrapolated isophote. On the other hand, when ghost pixels are turned on we get a smoothly curving isophote with no break.

A rigorous theoretical justification of the proceeding discussion is provided in our forthcoming paper [18]. Here we provide a partial analysis by looking at the continuum limit $h \rightarrow 0$ of u_h defined by (3.2) in the special case of weights $w(\mathbf{x}, \mathbf{y})$ given by (3.1), C^2 boundary data u_0 , a square inpainting domain, and $\mathbf{g}(\mathbf{x}) := \mathbf{g}$ constant. Specifically, we prove that as $h \rightarrow 0$ with $\epsilon/h := r$ fixed, u_h converges in L^∞ to a continuum limit u . In [18] we are able to relax the C^2 assumption to include, for

example, nowhere smooth boundary data with finitely many jump discontinuities. We also generalize our results to include convergence in L^p for general $1 \leq p \leq \infty$, finding in particular that if u_0 has jumps (across finitely many curves intersecting ∂D) then we can expect convergence in L^p for every $1 \leq p < \infty$, but *not* in L^∞ . We are also able to relate the rate of convergence to both the exponent p and the regularity of u_0 as quantified, for example, by the Hölder exponent of u_0 and its derivatives, if they exist (in general, convergence deteriorates as u_0 becomes less regular and p gets larger).

THEOREM 1. *Suppose $D_h = (0, 1]^2 \cap \mathbb{Z}_h^2$ equipped with periodic boundary conditions at $x = 0$ and $x = 1$, and supplied with C^2 boundary data $u_0 : (0, 1] \times (-\delta, 0] \rightarrow \mathbb{R}^d$, where $\delta > \epsilon > 0$. Suppose D_h is inpainted using a rule of the form*

$$(3.4) \quad u_h(\mathbf{x}) = \frac{\sum_{\mathbf{y} \in A_{\epsilon,h}(\mathbf{x}) \cap \Omega \setminus D} w(\mathbf{x}, \mathbf{y}) u_h(\mathbf{y})}{\sum_{\mathbf{y} \in A_{\epsilon,h}(\mathbf{x}) \cap \Omega \setminus D} w(\mathbf{x}, \mathbf{y})},$$

where $A_{\epsilon,h}(\mathbf{x}) \in \{B_{\epsilon,h}(\mathbf{x}), \tilde{B}_{\epsilon,h}(\mathbf{x})\}$, and $w(\mathbf{x}, \mathbf{y})$ given by (3.1) with $\mathbf{g}(\mathbf{x}) := \mathbf{g}$ constant

Then as $h \rightarrow 0$ with $r := \epsilon/h$ fixed, u_h converges in L^∞ with rate $O(h)$ to $u : (0, 1]^2 \rightarrow \mathbb{R}^d$ obeying the transport BVP

$$\nabla u \cdot \mathbf{g}^* = 0 \text{ on } (0, 1]^2, \quad u|_{y=0} = u_0|_{y=0}$$

where

$$(3.5) \quad \mathbf{g}^* = \frac{\sum_{\mathbf{y} \in A^-(\mathbf{0})} w(\mathbf{0}, \mathbf{y}) \mathbf{y}}{\sum_{\mathbf{y} \in A^-(\mathbf{0})} w(\mathbf{0}, \mathbf{y})} \quad A^-(\mathbf{0}) := \{(y_1, y_2) \in A_{\epsilon,h}(0) : y_2 < 0\}.$$

Proof. Here we prove the case where $A_{\epsilon,h}(\mathbf{x})$ contains no ghost pixels, that is $A_{\epsilon,h}(\mathbf{x}) \subset \mathbb{Z}_h^2$. For the case where $A_{\epsilon,h}(\mathbf{x})$ contains ghost pixels lying between pixel centers we refer the reader to [18]. We use the notation $\mathbf{x} := (ih, jh)$ interchangeably throughout.

First note that the symmetry of the situation allows us to rewrite (3.4) as

$$u_h(\mathbf{x}) = \frac{\sum_{\mathbf{y} \in A^-(\mathbf{0})} w(\mathbf{0}, \mathbf{y}) u_h(\mathbf{x} + \mathbf{y})}{\sum_{\mathbf{y} \in A^-(\mathbf{0})} w(\mathbf{0}, \mathbf{y})}.$$

Define $e_h := u_h - u$. Then it suffices to prove

$$(3.6) \quad |e_h(\mathbf{x})| \leq Ch$$

for all $\mathbf{x} \in D_h$, where $C > 0$ is a constant independent of \mathbf{x} . To prove this, we make use of the fact that since u is C^2 , there is a $D > 0$ s.t. $\|Hu\|_2 \leq D$ uniformly on $(0, 1]^2$, where Hu denotes the Hessian of u and $\|\cdot\|_2$ is usual operator norm induced by the vector 2-norm. We will use this to prove the stronger condition

$$(3.7) \quad |e_h(ih, jh)| \leq jDh^2,$$

from which (3.6) follows since $j \leq 1/h$.

We proceed by induction, supposing that (3.7) holds for all $(i'h, j'h)$ with $j' < j$ (the base case $j = 0$ is obvious). Applying our inductive hypothesis and expanding u

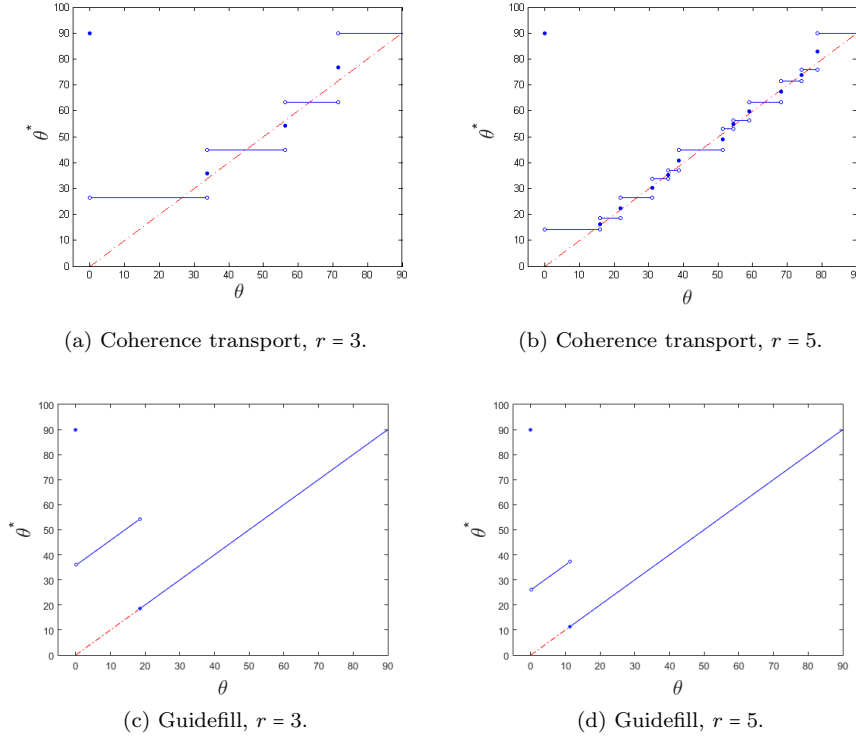


Fig. 7: The theoretical limiting curves $\theta^* = \theta(\mathbf{g}^*)$ given by (3.5) as a function of $\theta = \theta(\mathbf{g})$, for coherence transport (a)-(b) and Guidefill (c)-(d), for $r := \epsilon/h = 3, 5$, in the limit $\mu \rightarrow \infty$. Here \mathbf{g}^* is the theoretical limiting transport direction given in Theorem 1, while \mathbf{g} is the desired transport direction fed into the weights (3.1). The ideal curve $\theta^* = \theta$ (no kinking) is highlighted in red. Note that coherence transport exhibits kinking for all but finitely many angles, whereas Guidefill has no kinking for all angles greater than a critical minimum - see [18] for more details.

to second order we obtain:

$$\begin{aligned}
 |e_h(ih, jh)| &\leq \frac{\sum_{\mathbf{y} \in A^-(\mathbf{0})} w(\mathbf{0}, \mathbf{y}) |e_h(\mathbf{x} + \mathbf{y})|}{\sum_{\mathbf{y} \in A^-(\mathbf{0})} w(\mathbf{0}, \mathbf{y})} + \frac{\sum_{\mathbf{y} \in A^-(\mathbf{0})} w(\mathbf{0}, \mathbf{y}) |u(\mathbf{x} + \mathbf{y}) - u(\mathbf{x})|}{\sum_{\mathbf{y} \in A^-(\mathbf{0})} w(\mathbf{0}, \mathbf{y})} \\
 &\leq (j-1)Dh^2 + \nabla u(\mathbf{x}) \cdot \frac{\sum_{\mathbf{y} \in A^-(\mathbf{0})} w(\mathbf{0}, \mathbf{y}) \mathbf{y}}{\sum_{\mathbf{y} \in A^-(\mathbf{0})} w(\mathbf{0}, \mathbf{y})} + Dh^2 \\
 &= jDh^2 + \underbrace{\nabla u(\mathbf{x}) \cdot \mathbf{g}^*}_{=0}.
 \end{aligned}$$

Figure 7 illustrates the significance of Theorem 1 by plotting the phase $\theta(\mathbf{g}^*)$ of the theoretical limiting transport direction (3.5) as a function of the phase $\theta(\mathbf{g})$ of the input direction \mathbf{g} . The cases $\epsilon = 3h$ and $\epsilon = 5h$ are considered (coherence transport [7] recommends $\epsilon = 5h$ by default) with $\mu \rightarrow \infty$. For coherence transport we have $\theta(\mathbf{g}^*) \neq \theta(\mathbf{g})$ except for finitely many angles - this is consistent with numerical experiments. On the other hand, for Guidefill we have $\theta(\mathbf{g}^*) = \theta(\mathbf{g})$ for all angles

greater than a minimum value. We refer the reader to [18] for a full proof and for additional details.

REMARK 2. *The limiting transport direction \mathbf{g}^* predicted by Theorem 1 is similar to the transport direction predicted by März in [7] (Theorem 1). The key difference is that while März considered the double limit where $h \rightarrow 0$ and then $\epsilon \rightarrow 0$, we consider the single limit $(h, \epsilon) \rightarrow (0, 0)$ with $r = \epsilon/h$ fixed, which we argue in [18] is more relevant. The result is that whereas [7] obtains a formula for \mathbf{g}^* as an integral over a (continuous) half-ball, our \mathbf{g}^* is a finite sum over a discrete half-ball. In particular, when $A_{\epsilon,h}(\mathbf{x}) = B_{\epsilon,h}(\mathbf{x})$ as in coherence transport, the following predictions are obtained for the limiting transport direction:*

$$\mathbf{g}_{\text{März}}^* = \int_{\mathbf{y} \in B_1^-(\mathbf{0})} w(\mathbf{0}, \mathbf{y}) \mathbf{y} d\mathbf{y} \quad \mathbf{g}_{\text{ours}}^* = \sum_{\mathbf{j} \in b_r^-} w(\mathbf{0}, \mathbf{j}) \mathbf{j},$$

where

$$B_1^-(\mathbf{0}) := \{(x, y) \in \mathbb{R}^2 : x^2 + y^2 \leq 1 \text{ and } y < 0\}$$

$$b_r^- := \{(n, m) \in \mathbb{Z}^2 : n^2 + m^2 \leq r^2 \text{ and } m < 0\}.$$

Our discrete sum $\mathbf{g}_{\text{ours}}^*$ predicts the kinking observed by coherence transport in practice, whereas the integral $\mathbf{g}_{\text{März}}^*$ does not.

3.3. Automatic Spline Detection. The goal of the automatic spline detection is to position splines as straight lines in areas near the inpainting domain where we have detected a strong edge. These splines are lengthened so that they extend into the inpainting domain, and may be edited by the user before being used to construct the guide field.

A one pixel wide ring is computed a small distance from the inpainting domain. We then run a version of Canny edge detection [9] on an annulus of pixels containing the ring, and check to see which pixels on the ring intersect a detected edge. Portions of the annulus not labeled as belonging to the current object are ignored. For those pixels which do intersect a detected edge, we draw a spline in the direction of the edge beginning at that pixel and extending linearly into the inpainting domain.

The automatically detected splines can then be edited by the user to create the guide field \mathbf{g} as in Figure 3.

3.4. Automatic Determination of a Good Pixel Order (Smart Order).

Figure 8(a) and (c) shows the result of inpainting using a “onion shell” fill order (where pixels are filled as soon as they appear on the boundary of the inpainting domain), for a synthetic and non-synthetic example. In these cases extrapolated lines are cut off due to certain pixels being filled too early. Figure 8(b) and (d) shows the same examples using an improved fill order where these pixels are forced to wait for relevant information to reach them before being filled. We obtain orderings such as one used to generate 8(b) automatically by using the precomputed guide field to test, for each $\mathbf{x} \in \partial D_h$, whether or not the current iteration is a good time to fill \mathbf{x} . Specifically, to each $\mathbf{x} \in \partial D_h$ we assign a non-negative measure $m_{\mathbf{x}}$ defined by

$$m_{\mathbf{x}}(A) = \sum_{\mathbf{y} \in A} w(\mathbf{x}, \mathbf{y})$$

for any $A \subset \Omega$ and where $w(\mathbf{x}, \mathbf{y})$ is the weight function (3.1) depending implicitly on \mathbf{g} .

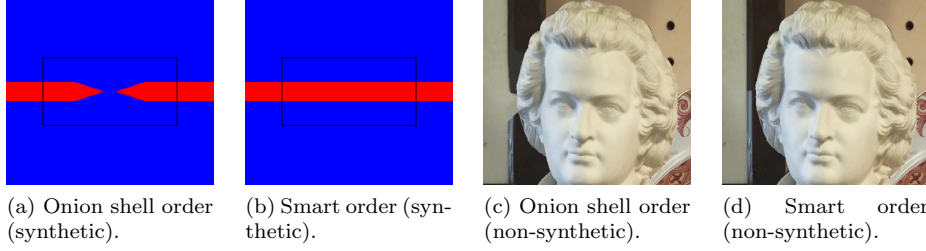


Fig. 8: Importance of Pixel Order: When pixels are filled in a simple “onion shell” order (i.e. filled as soon as they appear on the boundary of the inpainting domain), this creates artifacts including “clipping” of isophotes. Our smart order avoids this by using information from the pre-computed guide field to automatically decide when pixels should be filled. This is an advantage of our method in comparison with coherence transport [7], which computes “guides” concurrently with the inpainting. Here we illustrate with a synthetic and a non-synthetic example.

Then, before filling a given pixel $\mathbf{x} \in \partial D_h$ we check that the measure of the partial ball $\tilde{B}_{\epsilon,h}(\mathbf{x}) \cap \Omega \setminus (D \cup B)$ is at least some small, fixed fraction of the measure of the full ball $\tilde{B}_{\epsilon,h}(\mathbf{x})$, and if not wait until it is. That is, we check that

$$(3.8) \quad m_{\mathbf{x}}(\tilde{B}_{\epsilon,h}(\mathbf{x}) \cap \Omega \setminus (D \cup B)) \geq c m_{\mathbf{x}}(\tilde{B}_{\epsilon,h}(\mathbf{x})),$$

where $c \in (0, 1)$ is a small user specified constant ($c = 0.05$ by default).

Comparison with adapted distance functions for coherence transport

Note that our smart order cannot be straightforwardly incorporated into coherence transport, as it relies on the guide field being known prior to inpainting. In coherence transport $\mathbf{g}(\mathbf{x})$ is computed concurrently with inpainting and exhibits a similar sensitivity to the fill order.

In [22] März considers improved orderings for coherence transport based on a number of heuristics. Of these, the most similar to ours is the modified distance to boundary that orders points based on their distance from

$$\Gamma := \{\partial D_h : \langle \mathbf{g}(\mathbf{x}), \mathbf{N}(\mathbf{x}) \rangle^2 > \gamma\}$$

where $\mathbf{N}(\mathbf{x})$ denotes the normal to ∂D_h and $\gamma > 0$ is a user supplied constant. While this approach can also generate impressive results, it relies on a suitable definition of $\mathbf{N}(\mathbf{x})$, which may be awkward for general inpainting domains with irregular boundaries.

3.5. GPU Implementation. Some care is required in order to obtain a maximally efficient GPU implementation. In particular, some thought needs to go into how to assign threads to pixels, as well as how to cut down on memory accesses when working with ghost pixels. Here we go over two optimizations which together can lead to a speedup by an order of magnitude or more.

Efficient Implementation of Ghost Pixels. The core of our algorithm is the computation of $u_h(\mathbf{x})$ as a weighted sum of $u_h(\mathbf{y})$ over all “available” ghost pixels \mathbf{y} in the rotated ball $\tilde{B}_{\epsilon,h}(\mathbf{x})$ in Figure 4(b). Since ghost pixels are computed based

on bilinear interpolation (3.3) of their (up to) four nearest neighbors² in Ω_h , being available means that all of the relevant neighbors have already been “filled”. The naive approach to checking availability therefore requires up to four memory accesses per ghost pixel.

We reduce this to one (effective) memory access by taking advantage of the ability of most graphics cards to perform bilinear interpolation in hardware³. Specifically, we flag pixels as “filled” by writing a zero into their alpha channel. If a pixel is not filled, then we ensure that the alpha channel is at least 1. Since the bilinear interpolant of a non-negative function is zero at a point if and only if it is also zero at all neighboring (contributing) lattice points, we can determine if a ghost pixel \mathbf{y} is available simply by evaluating the alpha channel at \mathbf{y} using (hardware based) interpolation. If the result is zero, \mathbf{y} is available - otherwise it is not. Experiments indicate that this small change leads to a speed up by a factor of roughly four.

Boundary Tracking for Efficient Assignment of Threads to Pixels.

While early GPU programming languages such as GLSL leave programmers writing image processing code with little explicit control over the correspondence between threads and pixels, modern languages like CUDA and OpenCL assume no a priori connection between the two. These languages simply assign each thread a unique index (either an integer or tuple of integers) and leave it up to the programmer to decide how these indices map to pixels. This flexibility may be exploited for additional performance gains.

A naive approach is to assign one thread per pixel, however this is inefficient as only the boundary pixels are actually being updated. Since a typical HD image contains millions of pixels but the maximum number of concurrent threads in a typical GPU is in the tens of thousands⁴, this approach wastes a great deal of time in which the GPU is busy processing pixels that do not actually change.

A better approach is to assign threads only to pixels on the boundary of the inpainting domain, by maintaining a list of the coordinates of all boundary pixels. This list is updated every iteration by a parallel algorithm that requires each of $O(|\partial D_h|)$ threads to do logarithmic work.

Our algorithm is based on the observation that every boundary pixel at step k of Guidefill either was also a boundary pixel at step $k - 1$, or else has an immediate neighbor that was. More precisely, if $D_h^{(k-1)}$ and $D_h^{(k)}$ denote the inpainting domain at steps $k - 1$ and k respectively, then we can construct $\partial D_h^{(k)}$ as follows: For each $\mathbf{x} \in \partial D_h^{(k-1)}$, if $\mathbf{x} \in D_h^{(k)}$ then we insert \mathbf{x} into $\partial D_h^{(k)}$. On the other hand, if $\mathbf{x} \notin D_h^{(k)}$, then we iterate through the eight immediate neighbors in $\mathcal{N}(\mathbf{x})$ and add to $\partial D_h^{(k)}$ all neighbors which belong to $D_h^{(k)}$. This will result in a list which contains all pixels in the new boundary, but additionally contains some duplicates as a given pixel in $\partial D_h^{(k)}$ will in general be the neighbor of more than one pixel in $\partial D_h^{(k-1)}$. These duplicates

²If a ghost pixel happens to lie exactly on the vertical or horizontal line joining two pixel centers, then only two neighbors are required.

³Experiments indicate that bilinear interpolation in hardware (implemented in CUDA as a single texture lookup at a non-pixel center) is about four times faster than making four separate texture lookups at each of the nearest pixel centers and then performing the interpolation in software. However, we have been unable to find a reference explaining why this is so.

⁴For example, the GeForce GTX Titan X is a flagship NVIDIA GPU at the time of writing and has a total of 24 multiprocessors [2] each with a maximum of 2048 resident threads [26, Appendix G.1].

may then be eliminated using a standard parallel algorithm such as the one presented in [35, Ch. 10].

Rather than eliminate duplicates in post processing, we use a slightly more complex variant of the above approach that prevents duplicates before they occur. Details are given in the supplementary material.

4. Algorithmic Complexity. In this section we analyze the complexity of Guidefill as a parallel algorithm with and without boundary tracking. Specifically, we analyze how both the *time complexity* $T(N, M)$ and *processor complexity* $P(N, M)$ vary with $N = |D_h|$ and $M = |\Omega_h \setminus D_h|$, where a time complexity of $T(N, M)$ and processor complexity of $P(N, M)$ means that the algorithm can be completed by $O(P(N, M))$ processors in $O(T(N, M))$ time per processor. See for example [29, Ch. 5] for a more detailed discussion of the time and processor complexity formalism for parallel algorithms.

We assume that Guidefill is implemented on a parallel architecture consisting of p processors working at the same time in parallel. We further assume that when Guidefill attempts to run $P > p$ parallel threads such that there are not enough available processors to comply, the P threads are run in $\lceil P/p \rceil$ sequential steps. In reality, GPU architecture is not so simple - see for example [26, Ch. 4] for a discussion of GPU architecture, and for example [21] for a more realistic theoretical model. We do not consider these additional complexities here.

In Theorem 3 we derive a relationship between the time and space complexities $T(N, M)$, $P(N, M)$ and the number of iterations $K(N)$ required for Guidefill to terminate. This relationship is valid in general but does not allow us to say anything about $K(N)$ itself. Next, in Theorem 4 we establish bounds on $K(N)$ under a couple of simplifying assumptions. Firstly, we assume that the inpainting domain is surrounded entirely by readable pixels - that is $(\partial_{\text{outer}} D_h) \cap B_h = \emptyset$. In particular this means that we assume the inpainting domain does not include the edge of the image and is not directly adjacent to pixels belonging to another object (such as an object in the foreground). Secondly, we assume that the smart ordering of Section 3.4 is turned off (or equivalently, that no splines are being used to guide the inpainting). As neither of these assumptions are realistic, we also include a discussion in Section 4.1 of what to expect in the general case, but do not attempt a rigorous analysis. Our analysis considers only the filling step of Guidefill after the guide field has already been constructed.

THEOREM 3. *Let $N = |D_h|$, $M = |\Omega_h \setminus D_h|$ denote the problem size and let $T(N, M)$ and $P(N, M)$ denote the time complexity and processor complexity of the filling step of Guidefill implemented on a parallel architecture as described above with p available processors. Let $K(N)$ denote the number of iterations before Guidefill terminates. Then the processor complexity of Guidefill with and without boundary tracking is given by*

$$P(N, M) = \begin{cases} O(N + M) & \text{without tracking} \\ O(\sqrt{N} + M) & \text{with tracking} \end{cases}$$

while the time complexity is give by

$$T(N, M) = \begin{cases} O(K(N)) & \text{if } P(N, M) \leq p \\ O((N + M)K(N)) & \text{if } P(N, M) > p \end{cases} \quad \text{without tracking}$$

$$T(N) = \begin{cases} O((\sqrt{N} + K(N)) \log(N)) & \text{if } P(N, M) \leq p \\ O((N + K(N)) \log(N)) & \text{if } P(N, M) > p \end{cases} \quad \text{with tracking.}$$

Proof. For the case of no boundary tracking Guidefill allocates one thread per pixel in Ω_h , hence $P(N, M) = O(|\Omega_h|) = O(N + M)$. In this case if $|\Omega_h| := N + M < p$, then each thread fills only one pixel, and hence does $O(1)$ work. On the other hand, if $N + M > p$, each thread must fill $\lceil \frac{N+M}{p} \rceil$ pixels. It follows that

$$T(N, M) \leq \sum_{k=1}^{K(N)} \left\lceil \frac{N+M}{p} \right\rceil \leq \begin{cases} K(N) & \text{if } N+M < p \\ \frac{2}{p}(N+M)K(N) & \text{otherwise.} \end{cases}.$$

On the other hand, Guidefill with tracking allocates $O(|\partial D_h^{(k)}|)$ threads per iteration of Guidefill, each of which do $O(\log |\partial D_h^{(k)}|)$ work. This is because, as stated in Section 3.5, the boundary is updated over a series of $O(\log |\partial D_h^{(k)}|)$ parallel steps. In order to keep the processor complexity at $O(\sqrt{N+M})$, we assume that in the unlikely event that more than $\sqrt{N+M}$ threads are requested, then Guidefill runs them in $O\left(\left\lceil \frac{|\partial D_h^{(k)}|}{\sqrt{N+M}} \right\rceil\right)$ sequential steps each involving $\sqrt{N+M}$ processors. We therefore have, for $\sqrt{N+M} < p$

$$T(N, M) \leq \sum_{k=1}^{K(N)} \left(\frac{|\partial D_h^{(k)}|}{\sqrt{N+M}} + 1 \right) C \log |\partial D_h^{(k)}| \leq C \log(N) \sum_{k=1}^{K(N)} \left(1 + \frac{|\partial D_h^{(k)}|}{\sqrt{N+M}} \right)$$

where the factor $C > 0$ comes from the hidden constants in the Big O notation. But we know that $\{\partial D_h^{(k)}\}_{k=1}^{K(N)}$ form a partition of D_h , so that

$$\sum_{k=1}^{K(N)} |\partial D_h^{(k)}| = N.$$

Therefore

$$T(N, M) \leq C \log(N) \left(K(N) + \frac{N}{\sqrt{N+M}} \right) \leq C(\sqrt{N} + K(N)) \log(N).$$

An analogous argument with $\sqrt{N+M}$ in the denominator replaced by p handles the case $P(N, M) > p$.

THEOREM 4. *If we make the same assumptions as in Theorem 3 and if we further suppose $(\partial_{\text{outer}} D_h) \cap B_h = \emptyset$ and the smart order test from Section 3.4 is turned off, then we additionally have*

$$(4.1) \quad K(N) = O(\sqrt{N})$$

so that, in particular, we have $T(N, M) = O(\sqrt{N})$, $T(N, M) = O(\sqrt{N} \log(N))$ for Guidefill without and with tracking given sufficient processors, and $T(N, M) = O((N+M)\sqrt{N})$, $T(N, M) = O(N \log(N))$ respectively when there is a shortage of processors.

Proof. Now assume $(\partial_{\text{outer}} D_h) \cap B_h = \emptyset$ and (3.8) is disabled. Then after k iterations all pixels \mathbf{x} such that $\mathcal{N}^{(k)}(\mathbf{x}) \cap \Omega_h \setminus D_h \neq \emptyset$ will have been filled, where

$$\mathcal{N}^{(k)}(\mathbf{x}) = \bigcup_{\mathbf{y} \in \mathcal{N}^{(k-1)}(\mathbf{y})} \mathcal{N}(\mathbf{y}), \quad \mathcal{N}^{(1)}(\mathbf{x}) = \mathcal{N}(\mathbf{x}).$$

Therefore, if D_h has not be completely filled after k iterations, there must exist a pixel $\mathbf{x}^* \in D_h$ such that $\mathcal{N}^{(k)}(\mathbf{x}^*) \subseteq D_h$. However, it is easy to see that $|\mathcal{N}^{(k)}(\mathbf{x}^*)| =$

$(2k+1)^2$. But since $|D_h| = N$, after $k = \lceil \sqrt{N}/2 \rceil$ iterations $\mathcal{N}^{(k)}(\mathbf{x}^*)$ will contain more pixels than D_h itself, and cannot possibly be a subset of the latter.

This proves that Guidefill terminates in at most $\lceil \sqrt{N}/2 \rceil$ iterations, and hence $K(N) = O(\sqrt{N})$. \square

4.1. The general case. If we relax any of the additional assumptions in Theorem 4 then it ceases to be true in general. For example, if we eliminate the assumption that B_h is surrounded by readable pixels then $K(N)$ is no longer bounded above by $\lceil \sqrt{N}/2 \rceil$ and is instead given by

$$K(N) = \max_{\mathbf{x} \in D_h} \min_{\mathbf{y} \in \Omega_h \setminus (D_h \cup B_h)} d_{\mathcal{G}}(\mathbf{x}, \mathbf{y}),$$

where $d_{\mathcal{G}}(\mathbf{x}, \mathbf{y})$ is equal to the length of the shortest path in the graph \mathcal{G} with vertex set $\mathcal{V} = \Omega_h \setminus B_h$ and where each vertex $\mathbf{x} \in \mathcal{V}$ is connected to each of its (up to eight) neighbors in $\mathcal{N}(\mathbf{x}) \cap \mathcal{V}$. This can be as bad as $O(N)$ - consider, for example, an inpainting domain that is one pixel tall and N pixels wide, with just a single readable boundary pixel on one side and all other pixels within an annulus of width ϵ pixels surrounding the inpainting domain non-readable. If we take that one pixel away, then the runtime becomes infinite⁵. On the other hand, if we retain the assumption $(\partial_{\text{outer}} D_h) \cap B_h = \emptyset$ but turn on the smart order, we run into similar problems. The case where both assumptions are relaxed is even more complicated, but is related to the case of relaxing only one or the other by the following proposition:

PROPOSITION 5. *Let $K(N)$ denote the number of iterations required for Guidefill to terminate, and let $K_{\text{smart}}(N) \leq K(N)$ denote the last iteration on which the smart order test (3.8) causes the filling of a pixel to be delayed. Let $K^*(N)$ denote the number of iterations for Guidefill to terminate if the smart order test is disabled. Then*

$$(4.2) \quad K(N) \leq K_{\text{smart}}(N) + K^*(N)$$

Proof. After $K_{\text{smart}}(N)$ iterations, we will have filled a subset $\mathcal{V}^* \subseteq D_h$ of pixels and the smart order test (3.8) will no longer have any effect. The number of remaining iterations is therefore given by

$$\begin{aligned} K_{\text{remaining}}(N) &= \max_{\mathbf{x} \in D_h \setminus \mathcal{V}^*} \min_{\mathbf{y} \in (\Omega_h \setminus (D_h \cup B_h)) \cup \mathcal{V}^*} d_{\mathcal{G}}(\mathbf{x}, \mathbf{y}) \\ &\leq \max_{\mathbf{x} \in D_h} \min_{\mathbf{y} \in \Omega_h \setminus (D_h \cup B_h)} d_{\mathcal{G}}(\mathbf{x}, \mathbf{y}) \\ &= K^*(N). \end{aligned}$$

Although each of the quantities on the RHS of (4.2) are difficult to bound in general, we can obtain rough estimates under modest assumptions. In particular, as long as the splines are laid out in a reasonable way with one endpoint in the readable portion of the image $\Omega_h \setminus (D_h \cup B_h)$ and the other in D_h , such that none of the splines overlap the non-readable pixels in B_h and they are all spaced far enough apart that they do not cross or otherwise interact, then we expect that

$$K_{\text{smart}}(N) \lesssim \text{length in pixels of the longest spline.}$$

At the same time, we expect that the inpainting domains arising in 3D conversion will typically consist *mostly* of horizontal line segments with a readable pixel at one end

⁵In practice we implement checks to detect this case and terminate the algorithm.

and a non-readable pixel at the other. As we have already noted in Figure 2(c)-(d), it is also possible to have “cracks” with unreadable pixels on either side, however, so long as these cracks are not too deep we can expect

$$K^*(N) \lesssim \text{width in pixels of } D_h \text{ at its widest point.}$$

Excluding situations such as a very long and thin inpainting domain with a spline running down the entirety of its length, we typically expect both of these quantities to be much smaller than N , so that

$$K(N) \leq K_{\text{smart}}(N) + K^*(N) \ll N$$

in most cases in practice.

5. Numerical Experiments. In this section we aim to validate our method as a practical tool for 3D conversion, and also to validate the complexity analysis of Section 4. We have implemented Guidefill in CUDA C and interfaced with MATLAB. Our experiments were run on a laptop with a 3.28GHz Intel i7-4710 CPU with 20GB of RAM, and a GeForce GTX 970M GPU⁶.

3D Conversion Examples.

We tested our method on a number of HD problems, including the video illustrated in Figure 10 and the four photographs shown in Figure 9. The photographs were converted into 3D by building rough 3D geometry and creating masks for each object, as outlined in Section 2. For the movie, we used a computer generated model with existing 3D geometry and masks⁷, as generating these ourselves on a frame by frame basis would have been far too expensive (indeed, in industry this is done by teams of artists and is extremely time consuming). One advantage of this approach is that it gives us a ground truth to compare against, as in Figure 10(k). Please see also the supplementary material where our results can be viewed in video form, and in anaglyph 3d (anaglyph glasses required). Timings for Guidefill are given both with and without the boundary tracking algorithm described in Section 3.5.

For the photographs, we compare the output of Guidefill with five other inpainting methods - coherence transport [7, 22], the exemplar-based method of Criminisi et al. [14], the variational exemplar-based methods nl-means and nl-Poisson from Arias et al [3], and Photoshop’s Content-Aware fill. For the movie, we compare with the exemplar-based video inpainting method of Newson et al. [25, 24]. All methods are implemented in MATLAB + C (mex) and available for download online⁸.

Figure 10 shows a few frames of a 1280px × 960px × 101fr video, including the inpainting domain and the results of inpainting with both Guidefill and Newson’s method. With the exception of a few artifacts such as those visible in Figure 10(j), Newson’s method produces excellent results. However, it took 5hr37min to run, and

⁶The experiments involving nl-means and nl-Poisson are an exception. Because the implementation available online does not support Windows, these experiments had to be done on a separate Linux machine with a 3.40GHz Intel i5-4670 CPU with 16GB of RAM. As a comparison, we measured the time to solve a 500×500 Poisson problem to a tolerance of 10⁻⁶ using the conjugate gradient method in MATLAB, which took 8.6s on our Windows laptop, and 5.2s on the Linux box.

⁷Downloaded from <http://www.turbosquid.com/> in accordance with the Royalty Free License agreement.

⁸Coherence transport: <http://www-m3.ma.tum.de/bornemann/InpaintingCodeAndData.zip>, Criminisi’s method: https://github.com/ikuwow/inpainting_criminisi2004, nl-means and nl-Poisson: <http://www.ipol.im/pub/art/2015/136/>, Newson’s method: http://perso.telecom-paristech.fr/~gousseau/video_inpainting/.



(a) Wine



(b) Bust



(c) Pumpkin



(d) Planet

Fig. 9: Example photographs used for 3D conversion, of different sizes (a) 528×960 px (b) 1500×1125 px (c) 4000×4000 px (d) 5000×5000 px.

required more than 16GB of RAM. In comparison Guidefill produces a few artifacts, including the incorrectly completed window shown in Figure 10(e). In this case the failure is because the one pixel wide ring described in Section 3.3 fails to intersect certain edges we would like to extend. However, Guidefill requires only 19s (if boundary tracking is employed, 31s if it is not) to inpaint the entire video and these artifacts can be corrected as in Figure 10(f). However, due to the frame by frame nature of the computation, the results do exhibit some flickering when viewed temporally, an artifact which Newson’s method avoids.

Timings for the images are reported in Table 1, with the exception of Content-Aware fill which is difficult to time as we do not have access to the code. We also do not provide timings for Criminisi’s method, nl-means, and nl-Poisson for the “Pumpkin” and “Planet” examples as Criminisi ran out of memory while nl-means and nl-Poisson

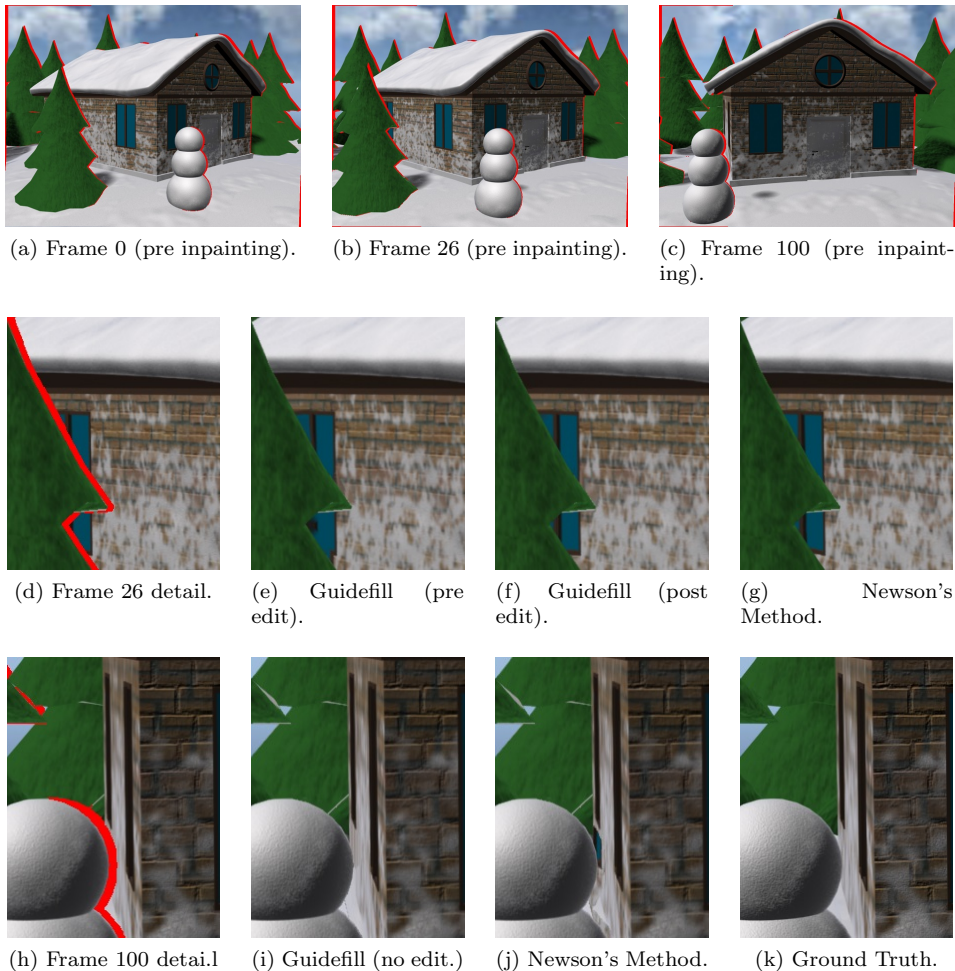


Fig. 10: Comparison of Guidefill (19s with tracking, 31s without) and Newson’s method (5hr37min) for inpainting the “cracks” (shown in red) arising in the 3d conversion of a HD video ($1280\text{px} \times 960\text{px} \times 101\text{fr}$). Guidefill produces artifacts such as the incorrectly extrapolated window in (e), but these can be corrected as in (f) and it is several orders of magnitude faster than Newson’s method (which also required more than 16GB of RAM in this case). The latter produces produces very high quality results, but is prohibitively expensive and still produces a few artifacts as in (j), which the user has no recourse to correct. A disadvantage of Guidefill is a flickering as the video is viewed through time due to the frames being inpainted independently. The video is provided in the online supplementary material.

did not finish within two hours. However, for the “Pumpkin” example we do provide the result of nl-Poisson run on a small region of interest. Results are given in Figures 11, 12, and 14. We do not show the output of every method and have included only the most significant.

The first example, “Wine”, is a $528 \times 960\text{px}$ photo. Timings are reported only for

the background object, which has an inpainting domain containing 15184px. Figure 13 shows the detected splines for the background object and illustrates the editing process. Results are then shown in Figure 11 in two particularly challenging areas. In this case the highest quality results are provided by nl-means and nl-Poisson, but both are relatively slow. Criminisi and Content-Aware fill each produce noticeable artifacts. Guidefill also has problems, most notably in the area behind the wine bottle, where the picture frame is extended incorrectly (this is due to a spline being too short) and where additional artifacts have been created next to the Chinese characters. These problems however are mostly eliminated by lengthening the offending spline and editing some of the splines in the vicinity of Chinese characters as illustrated in Figure 13. Guidefill is also the fastest method, although in this case the gains aren't as large as for bigger images.



(a) Detail one.



(b) Coherence transport - note the bending of the picture frame.



(c) nl-means - good result, but slow.



(d) nl-Poisson - Chinese characters are a solid block.



(e) Content-Aware Fill - distorted picture frame.



(f) Guidefill (before spline adjustment) - numerous issues.



(g) Guidefill (after adjustment) - issues are mostly resolved.



(h) Detail two.



(i) Criminisi - a piece of the picture frame is used to extrapolate the drawing.



(j) nl-Poisson - good result, but slow.



(k) Guidefill (before spline adjustment) - extension of drawing does not look natural.



(l) Guidefill (after adjustment) - more believable extrapolation.

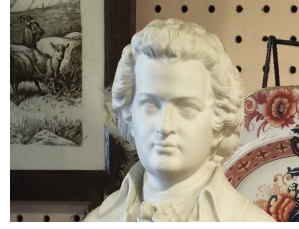
Fig. 11: Comparison of different inpainting methods for the “Wine” example. Two challenging areas are shown.



(a) Detail of “Bust”.



(b) Coherence transport.



(c) Content-Aware Fill.



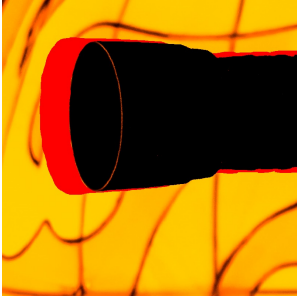
(d) nl-Poisson



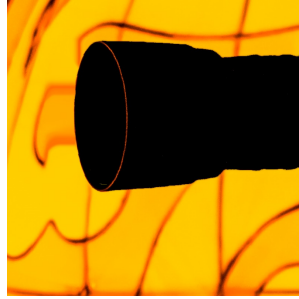
(e) Guidefill (before spline adjustment).



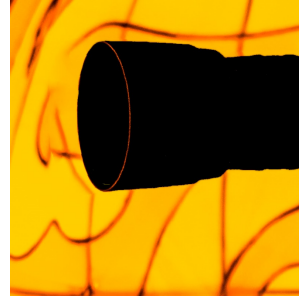
(f) Guidefill (after adjustment).



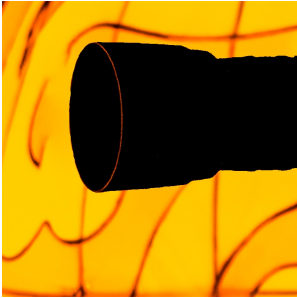
(g) Detail of “Pumpkin”.



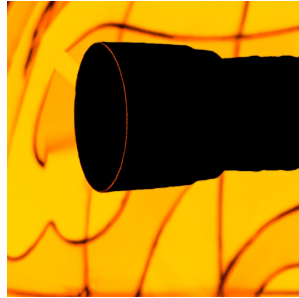
(h) coherence transport.



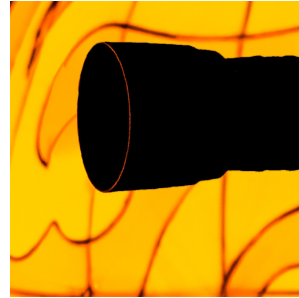
(i) Content-Aware Fill.



(j) nl-Poisson.



(k) Guidefill (before spline adjustment).



(l) Guidefill (after adjustment).

Fig. 12: Comparison of different inpainting methods for the “Bust” and “Pumpkin” examples.

Table 1: Timings of different inpainting algorithms used in the conversion of the three examples in Figure 9. The inpainting domains of “Wine”, “Bust”, and “Pumpkin” and “Planet” contain 15184px, 111277px, 423549px, and 1160899px respectively. “Guidefill n.t.” refers to guidefill without boundary tracking, and “C.T.” refers to coherence transport.

	C.T.	Crim	nl-means	nl-Poisson	Guidefill n.t.	Guidefill
Wine	340ms	1 min 40s	41s	2min11s	233ms	261ms
Bust	2.13s	37min	23min	1hr 10min	1.34s	559ms
Pumpkin	15.7s	–	–	–	6.66s	1.14s
Planet	28.5s	–	–	–	4.27s	923ms

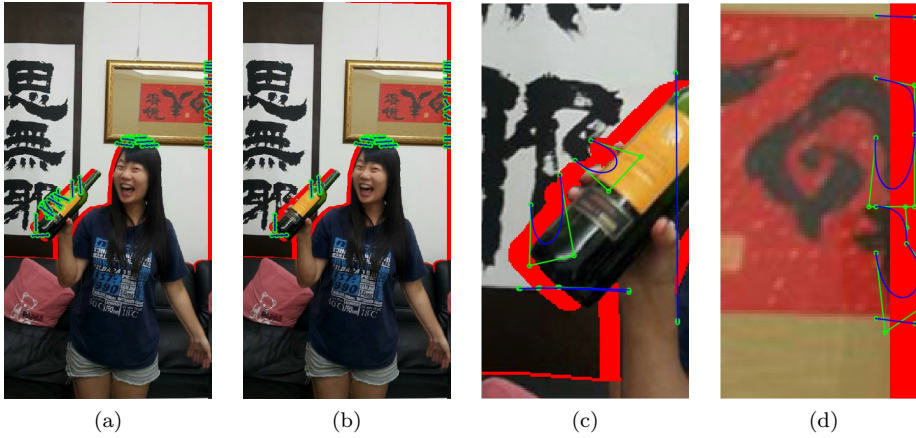


Fig. 13: Stages of spline adjustment for the “Wine” example: (a) The automatically detected splines for the background object. (b) Undesireable splines are deleted. (c) Deleted splines are replaced with new splines, drawn by hand, which form a plausible extension of the disoccluded characters. (d) Some of the remaining splines on the painting in the upper right corner are edited to form a more believable extension thereof.

The second example is a 1500×1125 px image. Timings are reported only for inpainting the background object, which has an inpainting domain containing 111277px, and results are shown in Figure 12(a)-(f). In this case we chose to edit the automatically detected splines, in particular rotating one that was crooked. Once again, the nicest result is probably nl-Poisson, but an extremely long computation time is required. All other algorithms, including Criminisi and nl-means which are not shown, left noticeable artifacts. The fully automatic version of Guidefill also leaves some artifacts, but these are largely eliminated by the adjustment of the splines.

Our third example is a very large 4000×4000 px image. Timings are reported only for the pumpkin object, which has an inpainting domain containing 423549px. Results are shown in Figure 12(g)-(l). We ran nl-Poisson on only the detail shown in Figure 12(g), because it did not finish within two hours when run on the image as a whole. In this case we edited the automatically detected splines as shown in Figure

3(a)-(b). In doing so we are able to recover smooth arcs that most fully automatic methods would struggle to produce. Guidefill in this case is not only the fastest method by far, it also produces the nicest result. In this example we also start to see the benefits of our boundary tracking algorithm, where it leads to a speed up of a factor of 2 – 3. In general we expect the gains from boundary tracking to be greater for very large images where the number of pixels is much larger than the number of available processors.

Our final example is a fun example that illustrates how 3D conversion may be used to create “impossible” 3D scenes. In this case the image is a 5000×5000 px “tiny planet” panorama generated by stitching together dozens of photographs. The choice of projection creates the illusion of a planet floating in space - however, in reality the center of the sphere is only a few feet from the camera, while its perimeter is at a distance of several kilometers. As a result, if this image were viewed in true 3D it would appear as an elongated “finger” rather than a round sphere. In order to preserve the illusion we created fake spherical 3D geometry. Results are shown in Figure 14. In this example the inpainting domain is relatively wide and the image is dominated by texture. As a result geometric methods are a bad choice and Guidefill - while fast - leaves noticeable artifacts. Content-Aware Fill does a better job and is more suitable for this case.

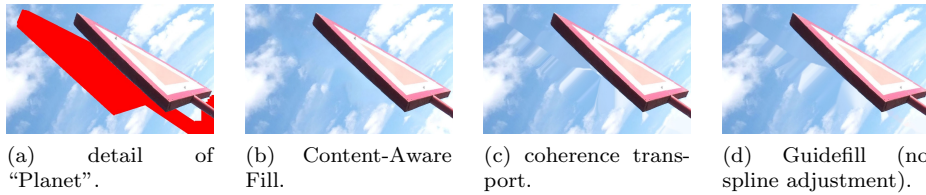


Fig. 14: Comparison of different inpainting methods for the “Planet” example. In this case geometric methods leave noticeable artifacts and exemplar-based methods like Content-Aware Fill are a better choice.

Validation of Complexity Analysis. As stated in Section 4, our analysis assumes that Guidefill is implemented on a parallel architecture consisting of p identical processors acting in parallel. In reality, NVIDIA GPUs contain a small number of multiprocessors, each of which issue one or two instructions to each of a small number of *warps* of 32 threads every clock cycle. For our particular GPU, this limits the number of threads that can receive instructions in a given clock cycle to 1280,⁹ in comparison with a maximum of 20480 threads that can be resident in the GPU at any given time¹⁰. However, because instructions take anywhere from tens to hundreds of clock cycles to execute, a GPU is able to keep a much larger number of threads “active” by issuing instructions to other warps in the intervening time. For simplicity, we assume in our analysis that p is equal to the maximum number of resident threads, that is $p = 20480$.

⁹10 multiprocessors times 4 warp schedulers per multiprocessor times 32 threads per warp.

¹⁰10 multiprocessors times 2048 maximum resident threads per multiprocessor.

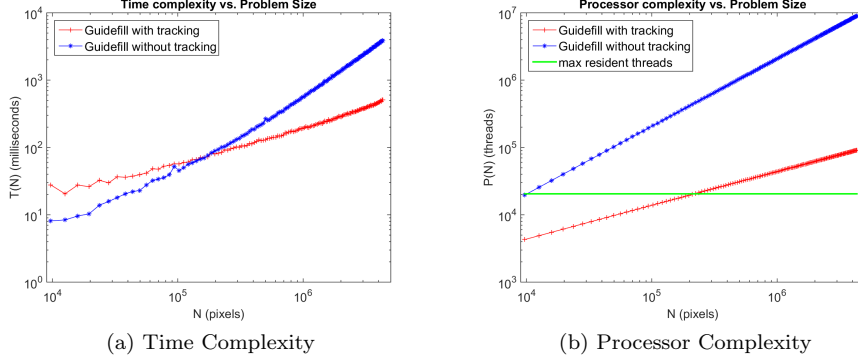


Fig. 15: **Experimental time complexity $T(N)$ and processor complexity $P(N)$ of Guidefill with and without boundary tracking:** The size of the inpainting domain varies from $N = |D_h| \approx 10^4 \text{px}$ up to $N = |D_h| \approx 10^6 \text{px}$, but the problems are identical up to scale. Results are given on a loglog scale to emphasize the approximate power law $T(N) \approx AN^\alpha$, $P(N) \approx BN^\beta$. A least squares fit gives $\alpha = 1.1$, $\beta = 1.0$ without tracking, and $\alpha = 0.54$, $\beta = 0.5$ with tracking. Despite the superior scaling law, the time complexity of Guidefill with tracking has a bigger hidden constant, meaning that for N small (e.g. $N \lesssim 2 \cdot 10^5 \text{px}$ in this case) performance is hurt. Processor complexity is compared with the maximum resident threads (green line), which provides a theoretical upper bound on the number of threads p that can be processed simultaneously.

We ran Guidefill on a series of synthetic problems similar to the one in Figure 5, consisting of a rectangular inpainting domain occluding a horizontal stripe. The size of the inpainting domain varied from $N \approx 10,000 \text{px}$ up to $N \approx 4,000,000 \text{px}$, but the problems were identical up to rescaling. In each case we measured the execution time $T(N)$ of Guidefill as well as the maximum number of threads $P(N)$, with and without tracking. Results are shown in Figure 15 - note the loglog scale. In Figure 15(b) we have also indicated the value of p for comparison - note that for Guidefill without tracking we have $P(N) \gg p$ for all but the smallest problems, but for Guidefill with tracking we have $P(N) < p$ up until $N \approx 2 \times 10^5$, after which $P(N)$ grows to no more than $5p$ (in comparison with $P(N) > 400p$ for Guidefill without tracking).

Based on Theorem 3 and Theorem 4 for Guidefill without tracking we expect $T(N) \in O(N^{1.5})$ for all N , but for Guidefill with tracking we expect $T(N) \in O(N^{0.5} \log(N))$ for N up to about 10^5px , with somewhat worse performance as N grows larger. To test these expectations we assume a power law of $T(N) \approx AN^\alpha$ (ignoring the factor of $\log(N)$) and solve for α by fitting a line to our data on a loglog plot. The results are $\alpha = 0.54$ and $\alpha = 1.10$ for Guidefill with and without tracking respectively (compared to $\alpha \approx 0.5$, $\alpha \approx 1.5$ expected), however, these change to $\alpha = 1.32$ and $\alpha = 0.65$ if all data points with $N < 10^6 \text{px}$ are discarded. Assuming a similar power law $P(N) \approx BN^\beta$ gives $\beta = 1.0$, $\beta = 0.5$ for Guidefill without and with tracking respectively.

These results imply that the analysis in Section 4 - despite being based on a highly simplistic model of GPU architecture - nonetheless does a reasonable job of predicting the behaviour of our method in practice. In particular, the superior scaling of Guidefill

with tracking is clearly demonstrated. While tracking actually reduces performance for very small problems, as the problem size grows the benefits of tracking become larger and larger, leading to a speed up by a factor of almost eight for the largest problems.

6. Conclusions. We have presented a fast inpainting method suitable for use in the hole-filling step of 3D conversion, which we call Guidefill. Guidefill is non-texture based, exploiting the fact that the inpainting domains in 3D conversion tend to be in the form of a thin “crack” such that texture can often be neglected. Its fast processing time and its setup allowing intuitive, user-guided amendment of the inpainting result render Guidefill into a user-interactive inpainting tool. A version of Guidefill is in use by the stereo artists at the 3D conversion company Gener8, where it has been used in major Hollywood blockbusters such as *Mockingjay*, *Pan*, and *Maleficent*.

Similarly to Telea’s Algorithm [34] and coherence transport [7, 22], Guidefill is based on the idea of filling the inpainting domain in shells while extrapolating isophotes based on a transport mechanism. However, we improve upon these methods in several important respects including the use of ghost pixels to alleviate kinking artifacts and the automatic computation of a good fill order. Also, as far as we know our method is the first parallel algorithm of this type.

In order to make our method as fast as possible we have implemented it on the GPU and proposed a couple of tricks to maximize performance. Firstly, we show in Section 3.5 how to take advantage of the GPU’s ability to perform bilinear interpolation in hardware in order to speed up certain computations, leading to an overall speed up by a factor of four. Second, we propose an algorithm to track the inpainting interface as it evolves, facilitating a massive reduction in the number of threads required by our algorithm. This does not lead to speed up by a constant factor - rather, it changes the complexity class of our method, leading to improvements that become arbitrarily large as $N = |D_h|$ increases. In practice we observed a slight decrease in speed for small images ($N \lesssim 10^5$ px), and gains ranging from a factor of 2 – 6 for larger images. We believe that variations of our boundary tracking algorithm could be used to speed up other image processing methods in which at any given time only a (small) subset of pixels are being changed. One example might be level set based image segmentation, which involves a similar evolving interface, assuming that changes to the level-set function far from the interface are small enough to be neglected.

A current disadvantage of our method is that, in order to keep execution times low, temporal information is ignored. In particular, splines are calculated for each frame separately, and inpainting is done on a frame by frame basis without consideration for temporal coherence. As a result of the former, artists must perform separate spline adjustments for every frame. In practice we find that only a minority of frames require adjustment, however one potential direction for improvement is to design a system that proposes a series of *animated* splines to the user, which they may then edit over time by adjusting control points and setting key frames. Secondly, a procedure for enforcing temporal coherence, if it could be implemented without significantly increasing the runtime, would be beneficial. However, these improvements are beyond the scope of the present work.

In those cases where it is suitable, especially scenes dominated by structure rather than texture and/or thin inpainting domains, Guidefill produces results that are competitive with alternative algorithms in a tiny fraction of the time, requiring under one second to inpaint more than one million pixels. In practice, Guidefill was found to be particularly useful for movies with many indoor scenes dominated by structure,

and less useful for movies taking place mainly outdoors, where texture dominates. Because of its speed, artists working on a new scene may apply our method first. If the results are unsatisfactory, they can edit the provided splines or switch to a more expensive method.

REFERENCES

- [1] <https://www.gener8.com/projects/>.
- [2] <http://www.geforce.co.uk/whats-new/articles/nvidia-geforce-gtx-titan-x>.
- [3] P. ARIAS, G. FACCIOLO, V. CASELLES, AND G. SAPIRO, *A variational framework for exemplar-based image inpainting*, Int. J. Comput. Vision, 93 (2011), pp. 319–347, doi:10.1007/s11263-010-0418-7, <http://dx.doi.org/10.1007/s11263-010-0418-7>.
- [4] C. BARNES, E. SHECHTMAN, A. FINKELSTEIN, AND D. GOLDMAN, *PatchMatch: A randomized correspondence algorithm for structural image editing*, ACM Transactions on Graphics (Proc. SIGGRAPH), 28 (2009).
- [5] M. BERTALMIO, G. SAPIRO, V. CASELLES, AND C. BALLESTER, *Image inpainting*, in Proceedings of the 27th annual conference on Computer graphics and interactive techniques, ACM Press/Addison-Wesley Publishing Co., 2000, pp. 417–424.
- [6] M. BERTALMIO, G. SAPIRO, V. CASELLES, AND C. BALLESTER, *Image inpainting*, in Proceedings of the 27th Annual Conference on Computer Graphics and Interactive Techniques, SIGGRAPH '00, New York, NY, USA, 2000, ACM Press/Addison-Wesley Publishing Co., pp. 417–424, doi:10.1145/344779.344972, <http://dx.doi.org/10.1145/344779.344972>.
- [7] F. BORNEMANN AND T. MÄRZ, *Fast image inpainting based on coherence transport*, Journal of Mathematical Imaging and Vision, 28 (2007), pp. 259–278, doi:10.1007/s10851-007-0017-6, <http://dx.doi.org/10.1007/s10851-007-0017-6>.
- [8] M. BURGER, L. HE, AND C. SCHÖNLIEB, *Cahn-hilliard inpainting and a generalization for grayvalue images*, SIAM J. Imaging Sci., 2 (2009), pp. 1129–1167.
- [9] J. CANNY, *A computational approach to edge detection*, IEEE Transactions on Pattern Analysis and Machine Intelligence, (1986).
- [10] F. CAO, Y. GOUSSEAU, S. MASNOU, AND P. PÉREZ, *Geometrically guided exemplar-based inpainting*, SIAM J. Img. Sci., 4 (2011), pp. 1143–1179, doi:10.1137/110823572.
- [11] T. CHAN, S. KANG, AND J. SHEN, *Euler’s elastica and curvature-based inpainting*, SIAM Journal on Applied Mathematics, (2002), pp. 564–592.
- [12] T. CHAN AND J. SHEN, *Variational image inpainting*, Communications on pure and applied mathematics, 58 (2005), pp. 579–619.
- [13] S. CHOI, B. HAM, AND K. SOHN, *Space-Time Hole Filling With Random Walks in View Extrapolation for 3D Video*, IEEE Transactions on Image Processing, 22 (2013), pp. 2429–2441, doi:10.1109/TIP.2013.2251646.
- [14] A. CRIMINISI, P. PÉREZ, AND K. TOYAMA, *Region filling and object removal by exemplar-based image inpainting*, IEEE Transactions on Image Processing, 13 (2004), pp. 1200–1212.
- [15] T. DOBBERT, *Matchmoving: The Invisible Art of Camera Tracking*, Sybex, Feb. 2005, <http://www.amazon.com/exec/obidos/redirect?tag=citeulike07-20&path=ASIN/0782144039>.
- [16] S. Z. . P. D. W. G. BRAVO, *Gpu-accelerated real-time free-viewpoint dibr for 3dtv*, IEEE Transactions on Consumer Electronics, 58 (2012), pp. 633 – 640, doi:10.1109/TCE.2012.6227470.
- [17] J. HERLING AND W. BROLL, *High-quality real-time video inpainting with pixmix*, IEEE Transactions on Visualization and Computer Graphics, 20 (2014), pp. 866–879, doi:doi.ieeecomputersociety.org/10.1109/TVCG.2014.2298016.
- [18] L. R. HOCKING, T. HOLDING, AND C.-B. SCHÖNLIEB, *A framework for the numerical analysis of a class of geometric image inpainting algorithms*.
- [19] A. KOKARAM, B. COLLIS, AND S. ROBINSON, *Automated rig removal with Bayesian motion interpolation*, Vision, Image and Signal Processing, IEE Proceedings -, 152 (2005), pp. 407–414, doi:10.1049/ip-vis:20045152, <http://dx.doi.org/10.1049/ip-vis:20045152>.
- [20] Y. LAI, Y. LAI, AND J. LIN, *High-quality view synthesis algorithm and architecture for 2d to 3d conversion*, in 2012 IEEE International Symposium on Circuits and Systems, ISCAS 2012, Seoul, Korea (South), May 20–23, 2012, 2012, pp. 373–376, doi:10.1109/ISCAS.2012.6272040, <http://dx.doi.org/10.1109/ISCAS.2012.6272040>.
- [21] L. MA, K. AGRAWAL, AND R. D. CHAMBERLAIN, *A memory access model for highly-threaded many-core architectures*, Future Generation Computer Systems, 30 (2014), pp. 202 – 215, doi:http://dx.doi.org/10.1016/j.future.2013.06.020, <http://www.sciencedirect.com/science/article/pii/S0167739X13001349>.
- [22] T. MÄRZ, *Image inpainting based on coherence transport with adapted distance functions*,

- SIAM J. Img. Sci., 4 (2011), pp. 981–1000, doi:10.1137/100807296, <http://dx.doi.org/10.1137/100807296>.
- [23] S. MASNOU AND J. MOREL, *Level lines based disocclusion*, in Image Processing, 1998. ICIP 98. Proceedings. 1998 International Conference on, IEEE, 1998, pp. 259–263.
 - [24] A. NEWSON, A. ALMANSA, M. FRADET, Y. GOUSSEAU, AND P. PÉREZ, *Towards fast, generic video inpainting*, in Proceedings of the 10th European Conference on Visual Media Production, CVMP '13, New York, NY, USA, 2013, ACM, pp. 7:1–7:8, doi:10.1145/2534008.2534019, <http://doi.acm.org/10.1145/2534008.2534019>.
 - [25] A. NEWSON, A. ALMANSA, M. FRADET, Y. GOUSSEAU, AND P. PÉREZ, *Video inpainting of complex scenes*, SIAM Journal on Imaging Sciences, 7 (2014), pp. 1993–2019, doi:10.1137/140954933.
 - [26] NVIDIA, *CUDA C Programming Guide*, 2015.
 - [27] K. OH, S. YEA, AND Y. HO, *Hole filling method using depth based in-painting for view synthesis in free viewpoint television and 3-d video*, in Proceedings of the 27th Conference on Picture Coding Symposium, PCS'09, Piscataway, NJ, USA, 2009, IEEE Press, pp. 233–236, <http://dl.acm.org/citation.cfm?id=1690059.1690118>.
 - [28] M. PHARR AND R. FERNANDO, *GPU Gems 2: Programming Techniques for High-Performance Graphics and General-Purpose Computation (Gpu Gems)*, Addison-Wesley Professional, 2005.
 - [29] S. H. ROOSTA, *Parallel processing and parallel algorithms : theory and computation*, Springer, New York, 2000, <http://opac.inria.fr/record=b1096260>.
 - [30] H. SAWHNEY, Y. GUO, J. ASMUTH, AND R. KUMAR, *Multi-view 3d estimation and applications to match move*, in Proceedings of the IEEE Workshop on Multi-View Modeling & Analysis of Visual Scenes, MVIEW '99, Washington, DC, USA, 1999, IEEE Computer Society, pp. 21–, <http://dl.acm.org/citation.cfm?id=519933.825159>.
 - [31] C.-B. SCHÖNLIEB, *Partial Differential Equation Methods for Image Inpainting*, 2015.
 - [32] M. SEYMOUR, *Art of stereo conversion: 2d to 3d.*, May 2012, <https://www.fxguide.com/featured/art-of-stereo-conversion-2d-to-3d-2012/>.
 - [33] J. SUN, L. YUAN, J. JIA, AND H. SHUM, *Image completion with structure propagation*, ACM Trans. Graph., 24 (2005), pp. 861–868, doi:10.1145/1073204.1073274, <http://doi.acm.org/10.1145/1073204.1073274>.
 - [34] A. TELEA, *An image inpainting technique based on the fast marching method*, Journal of Graphics Tools, 9 (2004), pp. 23–34.
 - [35] A. TUCKER, *Computer Science Handbook, Second Edition*, Chapman & Hall/CRC, 2004.
 - [36] J. WEICKERT, *Anisotropic Diffusion in Image Processing*, ECMI Series, Teubner, Stuttgart, 1998, <http://www.mia.uni-saarland.de/weickert/book.html>.
 - [37] Y. WEXLER, E. SHECHTMAN, AND M. IRANI, *Space-time completion of video*, IEEE Trans. Pattern Anal. Mach. Intell., 29 (2007), pp. 463–476, doi:10.1109/TPAMI.2007.60.
 - [38] X. XU, L. PO, C. CHEUNG, L. FENG, K. H. NG, AND K. W. CHEUNG, *Depth-aided exemplar-based hole filling for DIBR view synthesis*, in 2013 IEEE International Symposium on Circuits and Systems (ISCAS2013), Beijing, China, May 19-23, 2013, 2013, pp. 2840–2843, doi:10.1109/ISCAS.2013.6572470, <http://dx.doi.org/10.1109/ISCAS.2013.6572470>.
 - [39] J. ZHI, *A case of study for 3d stereoscopic conversion in visual effects industry*, International Journal of Computer, Electrical, Automation, Control and Information Engineering, 7 (2013), pp. 53 – 58, <http://iastem.com/Publications?p=73>.
 - [40] S. ZINGER, L. DO, AND P. DE WIT, *Free-viewpoint depth image based rendering*, J. Vis. Comun. Image Represent., 21 (2010), pp. 533–541, doi:10.1016/j.jvcir.2010.01.004, <http://dx.doi.org/10.1016/j.jvcir.2010.01.004>.